REPORT DOCUMENTATION PAGE

Form Approved OMB No. 0704-0188

Public reporting burden for this collection of information is estimated to average 1 hour per response, including the time for reviewing instructions, searching existing data sources, gathering and maintaining the data needed, and completing and reviewing the collection of information. Send comments regarding this burden estimate or any other aspect of this collection of information, including suggestions for reducing the burden, to Department of Defense, Washington Headquarters Services, Directorate for Information Operations and Reports (0704-0188), 1215 Jefferson Davis Highway, Suite 1204, Arlington, VA 22202-4302. Respondents should be aware that notwithstanding any other provision of law, no person shall be subject to any penalty for failing to comply with a collection of information if it does not display a currently valid OMB control number.
PLEASE DO NOT RETURN YOUR FORM TO THE ABOVE ADDRESS.

1. REPORT DATE *(DD-MM-YYYY)* 24-08-2005	2. REPORT TYPE Final Report	3. DATES COVERED *(From – To)* 1 June 2004 - 03-Mar-06

4. TITLE AND SUBTITLE

New Target Detection and Tracking Procedure using Spatially Extended Nonlinear Dynamical Systems (SENDSS)

5a. CONTRACT NUMBER
FA8655-04-1-3043

5b. GRANT NUMBER

5c. PROGRAM ELEMENT NUMBER

6. AUTHOR(S)

Dr. Weiping Lu

5d. PROJECT NUMBER

5d. TASK NUMBER

5e. WORK UNIT NUMBER

7. PERFORMING ORGANIZATION NAME(S) AND ADDRESS(ES)
Edinburgh Scientific Consultants
38 Ormidale Terrace
Edinburgh EH12 6EF
United Kingdom

8. PERFORMING ORGANIZATION REPORT NUMBER

N/A

9. SPONSORING/MONITORING AGENCY NAME(S) AND ADDRESS(ES)

EOARD
PSC 821 BOX 14
FPO 09421-0014

10. SPONSOR/MONITOR'S ACRONYM(S)

11. SPONSOR/MONITOR'S REPORT NUMBER(S)
Grant 04-3043

12. DISTRIBUTION/AVAILABILITY STATEMENT

Approved for public release; distribution is unlimited.

13. SUPPLEMENTARY NOTES

14. ABSTRACT

This report results from a contract tasking Edinburgh Scientific Consultants as follows: The Grantee will investigate the use of Spatially Extended Nonlinear Dynamical Systems (SENDS) for the development of a radically new target detection and tracking procedure. The research adopts a strategy of combining target tracking with detection, and has the potential for real-time and high-resolution operation using optical systems. This strategy stems from the similarity between the partial differential equation (PDEs) currently used for image processing in computer vision and those in optics to describe dynamics and complexity of spatially extended nonlinear systems. Specifically, the Grantee will
1)   investigate new PDE-based imaging algorithms that incorporate PDEs for image processing with those describing nonlinear spatiotemporal dynamics, demonstrate and characterize these algorithm for enhanced spatiotemporal filtering.
2)   analyze the dynamics of localized structure solutions of the SEND in the presence of image sequences, develop and characterize a new target-tracking procedure by incorporating the localized structure into the above PDE-based imaging algorithm.

15. SUBJECT TERMS
EOARD, Tracking, Optical systems, Mathematical Modeling

16. SECURITY CLASSIFICATION OF:			17. LIMITATION OF ABSTRACT UL	18, NUMBER OF PAGES	19a. NAME OF RESPONSIBLE PERSON DONALD J SMITH
a. REPORT UNCLAS	**b. ABSTRACT** UNCLAS	**c. THIS PAGE** UNCLAS		13	**19b. TELEPHONE NUMBER** *(Include area code)* +44 (0)20 7514 4953

Standard Form 298 (Rev. 8/98)
Prescribed by ANSI Std. Z39-18

New target detection and tracking procedure using
spatially extended nonlinear dynamical systems (SENDSs)

Final Report
(August 2004-July 2005)

by
W. Lu and R. G. Harrison
(August, 2005)

European Office of Aerospace Research and Development -EOARD

London, England

Contract Number FA8655-04-1-3043

I. Overview

Real-time image processing underpins many civil and military applications such as telescopic monitoring of celestial bodies in night sky, infrared surveillance, security and traffic monitoring and medical imaging. Finding a real-time solution for these tasks is nontrivial. High-resolution images can significantly slow down the processing rate, whereas data processing becomes difficult and time-consuming if the objects are of low contrast and cluttered. Many applications also impose constraints on the physical size, power requirement and cost of the solution. Moreover, in many situations the solution must be capable of reconfiguration and/or modification, which precludes dedicated hardware. For these reasons, real-time, high-resolution image processing remains an open problem in spite of intense effort spanning many decades.

Recently, spatially extended nonlinear dynamical systems (SENDSs) have been proposed for applications to image processing. This strategy stems from the similarity between the partial differential equation (PDEs) currently used for image processing in computer vision and those in optics to describe dynamics and complexity of spatially extended nonlinear systems. The intrinsic parallelism of optical systems has the potential for increased processing speed towards real-time and high-resolution operation.

This project has studied the novel spatiotemporal phenomena in a SENDS for the development of a radically new image processing methodology. This report comprises two parts for different applications: i) target detection and tracking and ii) wave-front sensing and image recovery, both are based essentially on the same principle of nonlinear information processing using SENDSs.

This document contains earlier results from the previous 3 interim report as well as new research results over the last 3 months.

II. Programme of Work

PART ONE: Target Detection and Tracking

1.1 Introduction

This work will demonstrate that optical systems may provide a real-time solution for image processing. We show that this possibility has come about through profound and radically new understanding of pattern formation and complexity in spatially extended nonlinear dynamical systems (SENDSs), which is now a major branch of nonlinear science. In optics, these pattern-forming systems are described by PDEs of similar form to those currently used for computer based image analysis. It follows therefore that SENDSs may be used for image processing based on the same PDE approach as described above. The critical point here is that an optical SENDS is an analogue device with massive parallelism and high speed, so capable of performing PDE processing in real time. As one example, we here focus on a novel approach **of** hybrid optoelectronic image processing, which offers unprecedented system flexibility and capability for real-time image processing.

1.2 Theoretical Model

Figure 1 shows the schematic of a SENDS, which can be implemented using opto-electronic architecture. The phase of the coherent input beam is modulated as it transmits through the phase spatial light modulator (SLM). The input beam then experiences a free-space propagation and is recorded on a photo-array for subsequent nonlinearity and spatial spectral filtering (electronic signal processing) before it is fed back to the SLM. The depth of the phase modulations is the sum of those induced by the (electronic) signal
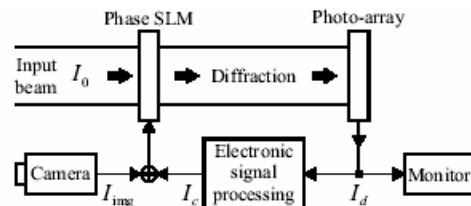

Fig. 1. Schematic of the hybrid nonlinear system.

intensities formed in the feedback loop, $u(\mathbf{r},t) \equiv \gamma I_c(\mathbf{r},t)$ and by the external images registered by the camera, $\phi(\mathbf{r},t) \equiv \gamma I_{img}(\mathbf{r},t)$ where $\mathbf{r}$ is the transverse radius vector, t the time, and the proportionality constant γ controls the depth of phase modulations. The dynamics of the phase modulation $u(\mathbf{r},t)[I_c(\mathbf{r},t)]$ in the feedback loop is described by the equation

$$\tau_0 \frac{\partial u(\mathbf{r},t)}{\partial t} + u(\mathbf{r},t) = D\nabla_\perp^2 u(\mathbf{r},t) + Kw_{FB}(\mathbf{r},t) \tag{1}$$

where τ_0 is the characteristic time determined by the iterating rate (frame upgrading) in the feedback loop and K the feedback gain coefficient which has incorporated γ. The feedback signal is a convolution integral of a nonlinear function $\Phi(I_d) = 2\exp(-4(I_d - 1)^2)$ and a low-pass spatial filter $h(\mathbf{r})$ of super-Gaussian shape with power α and a cut-off frequency q_{cut}. Here $I_d(\mathbf{r},\,t) = |A(\mathbf{r},\,z = L,\,t)|^2$ is the intensity distribution registered at the photo-array and normalized by a half of the maximum value of the input intensity I_0. The equation describing the input laser beam propagating over the distance L from the SLM to the photo-array is given as

$$-2ik_0 \frac{\partial A(\mathbf{r},z,t)}{\partial z} = \nabla_\perp^2 A(\mathbf{r},z,t) \tag{2}$$

with the boundary condition
$$A(\mathbf{r},z=0,t) = A_0 \exp[iu(\mathbf{r},t) + \phi(\mathbf{r},t)], \tag{3}$$
where A_0 is the amplitude of the incident optical wave. Equations (1-3) represent the mathematical model of the hybrid nonlinear system with control parameters I_0, K, and L.

1.3 Numerical simulation of detection of small moving objects

To demonstrate the capability of the model for detection of small moving targets, we have first numerically integrated Eqs.(1)-(3). Throughout our simulations we fix the cut-off frequency $q_{cut} = \sqrt{\pi}q_0$ and the power $\alpha = 8$ for the low-pass super-Gaussian spatial filter. For the analysis of the system's performance we use both statistically homogeneous and isotropic random functions, $b(\mathbf{r})$, as a background image. Specifically, we exploit the Gaussian model for the random function's spatial power spectrum $G(q)$, i.e.
$$G(q) = G_0 \exp\left(-q^2/2q_b^2\right),$$
where q_b is the characteristic spatial spectrum width. Example realisations of random functions $b(\mathbf{r})$ corresponding to the spectrum for two different values of q_b are shown in Fig.2(a) and (d). As seen, in the input images having a background of Gaussian spectrum of width $q_b = 0.5\sqrt{\pi/2}q_0$, the contribution of high spatial frequencies is more pronounced than that with $q_b = 0.25\sqrt{\pi/2}q_0$. To create the input image stream $I_{img}(\mathbf{r},t)$, we superimpose a single realisation of the random function $b(\mathbf{r})$ with a small object of Gaussian profile on a zero background moving with the constant velocity $\mathbf{v}$, i.e.:

$$I_{img}(\mathbf{r},t) = b(\mathbf{r}) + a_{tg}\exp\left\{-\left[\mathbf{r} - \mathbf{r}_{tg}(t)\right]^2 / 2d_{tg}^2\right\}, \tag{4}$$

where $\mathbf{r}$ is the radius vector in the transverse plane, $\mathbf{r}_{tg}(t) = \mathbf{r}'_{tg} + \mathbf{v}t$ the coordinate of the centre of the moving object, $\mathbf{r}'_{tg}$ the initial coordinate of the centre of the object, d_{tg} the width of the object and a_{tg} the amplitude of the object. The amplitude a_{tg} is chosen in such a way that it does not exceed the maximum

amplitude of the background function $b(\mathbf{r})$. The width of the moving object d_{tg} is inversely proportional to the characteristic spatial spectrum width of the object, $d_{tg} = 1/q_{tg}$, that is assumed to be equal to $q_{tg} = 0.5\sqrt{\pi/2}q_0$. The speed of the moving object is assumed to be equal to a one-pixel shift in both x and y directions in the transverse plane between successive frames. The output image for observation is the intensity distribution registered at the photo-array, $I_d(\mathbf{r},t)$. To estimate the effectiveness of nonlinear filtering by the system, we compare the output intensity with and without feedback by fixing the feedback gain coefficient K at -2 and 0, as shown in figure 2. It clearly shows that the background is much smoother in the presence of feedback for the both case, indicating strong performance of noise reduction. The moving-object detection efficiency can be quantitatively estimated using the visibility function $R(t)$, defined as

$$R(t) = \frac{I_d^{tg}(t) - \bar{I}_d(t)}{\sigma(t)}, \qquad (5)$$
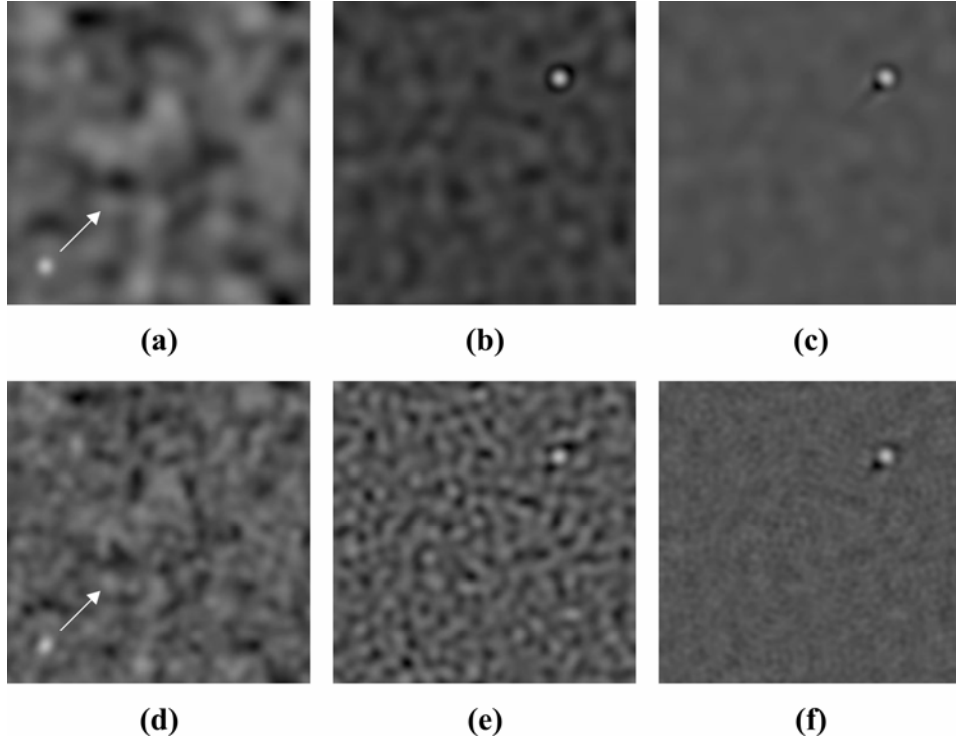

(a) **(b)** **(c)**

(d) **(e)** **(f)**

FIG. 2 Real-time detection of small moving object on Gaussian background image. (a) and (d) are snapshots of the input image stream $I_{img}(\mathbf{r},t=0)$ with $q_b = 0.25\sqrt{\pi/2}q_0$ and $q_b = 0.5\sqrt{\pi/2}q_0$, respectively; the direction of motion of the object with $q_{tg} = 0.5\sqrt{\pi/2}q_0$ is indicated by arrows. The traces (b, e) and (c, f) are snapshots of the output images $I_d(\mathbf{r},t=4\tau_0)$ in the system without ($K=0$) and with ($K=-2$) feedback, respectively. The value of the driving intensity I_0 is fixed at 0.5.

where $\sigma(t) = \sqrt{\dfrac{1}{S}\int [I_d^{tg}(\mathbf{r},t) - \bar{I}_d(t)]^2 d^2\mathbf{r}}$ is the feedback intensity variance averaged over the image frame area, $I_d^{tg}(t)$ the intensity value corresponding to the centre point of the moving target and $\bar{I}_d(t)$ the feedback intensity averaged over the image frame area S. We have found that our system increases the visibility of the object by five times in this case study.

1.4 Dynamics of localised state

We further investigate the dynamics of localised state in the SENDS and study its feasibility for target tracking. Fig. 3 (a) shows the dependence of the amplitude of LSs, obtained numerically, on the gain parameter K for a set of two values of the driving intensity I_0. The corresponding time duration needed for the formation of LSs is depicted in Fig.3(b). The time has been estimated for the amplitude of an LS to attain 90% of its full value. As seen from Fig.3 (b), it has a maximum at a certain value of K for a given I_0. This value indicates a boundary between linear and nonlinear growth of spatial perturbations leading to the formation of the LS and for convenience can be defined as the threshold value of K for the formation of the LS. As seen from the figure, above this threshold (the maximum point), the time duration for the formation of
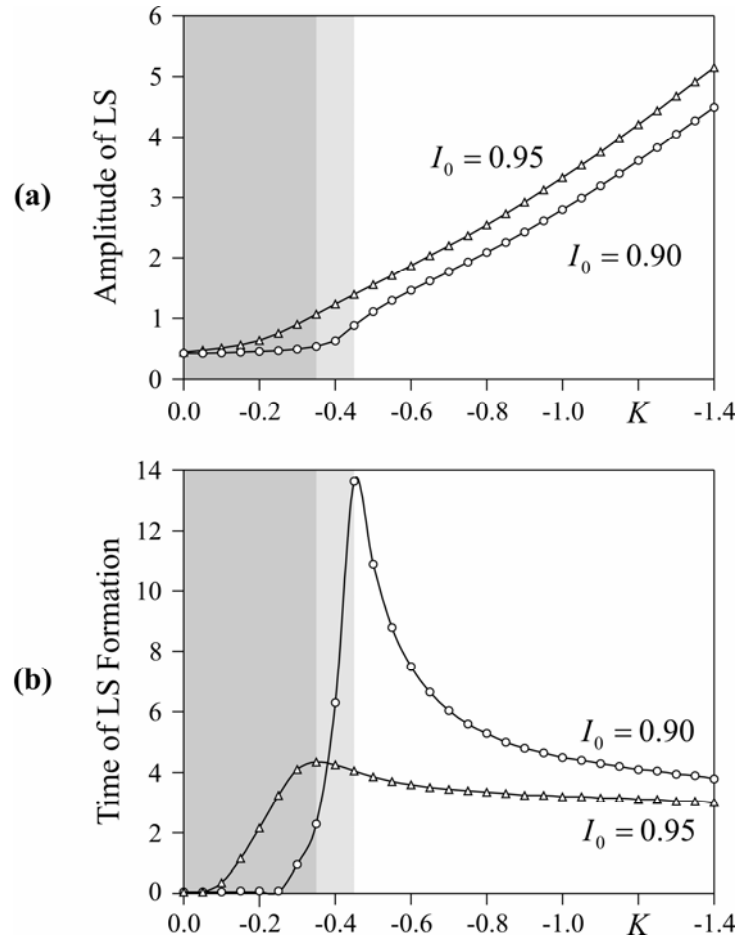

FIG.3. The amplitude of LS (a) and time formation of LS (b) dependences on gain parameter K for two different values of driving intensity I_0. The linear operation regions for $I_0 = 0.9$ and $I_0 = 0.95$ are shadowed by 10% and 20% black, respectively.

the LS decreases with the increase of $|K|$. This dependence gives us a possibility to control the dynamics of the system. Importantly, we find that in general the time required for background depression in the SENDS is much shorter than that for the formation of LSs. As such background noise can be depressed before LSs are formed in real target. The conclusion will be tested in the next phase of the programme.

1.5 Target detection and tracking

The work above has demonstrated that the SENDS has a stationary solution that minimizes the amplitude of the phase modulations. This solution can be used for background noise suppression. For moving objects in images a stationary state can not be reached and as a result these objects are "transparent" in the system. This leads to image enhancement of moving objects. The efficiency of suppression/enhancement of stationary/moving features in images are also spatial-frequency dependent, which leads to both space and time domain image processing. Along with these useful features, the system has a unique solution of localized states as it is a spatio-temporal dynamical system. The localized state can be controlled to track small moving objects. We have identified three critical features of LS's for the proposed tracking task. Firstly, LS formation has a threshold characteristic. Secondly, the time duration required for LS formation is generally considerably longer than that required for background suppression. The difference of these two time scales is critically important since cluttered background and nuisance objects can be first suppressed so that localized structures are excited only on the targets. Thirdly, the localized structures excited on the targets can move with the targets and so track their trajectories.

These three criteria have been demonstrated through a case study. As shown in Fig.4(a), the external image stream is based on a real scene of clouds at sunset, comprising as seen complex (static) spatial distributions of different scales. Two moving objects are added by computer; a fast-moving and small-size target and slow-moving and large-size nuisance object, both of them have comparable brightness with the background. We show that both the nuisance object and background are suppressed in the output of the system at the time of one round trip time, thus enhancing the contrast of the real target. After the suppression, only the target exceeds the threshold thus exciting a localized structure at its location. The threshold can be controlled by varying the parameter of the system. Fig.4(b) shows a snapshot of the processed image stream at the time of three round trip time when the cluttered background is suppress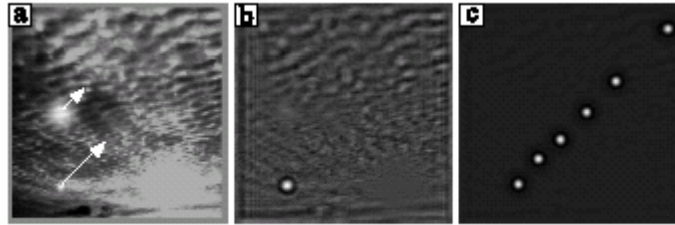ed and an LS is growing on the target. We have observed two different dynamical behaviors of the localized structure in the presence of a moving target; a single LS moving along

Fig.4. Simulation of detection and tracking of a small moving targets by use of LSs.

with the target or a sequence of localized spots [Fig. 4(c)] at moving target locations, both tracking the trajectory. The two operation modes correspond to targets of slow and fast speed, respectively, and can be selected and controlled by choosing a suitable time constant of the system. In this case study, the target visibility is further enhanced by ten times by using the localized structure.

1.6 Image edge enhancement

The theoretical model described above has been further developed to include an interferometer arm in the feedback loop for image edge enhancement. An intensity image under investigation is imported to the system as phase modulation (phase image) via a second SLM, the depth of which can be controlled by the system. The feedback signal is the sum of the intensity from the interferometer and that after free-space propagation in the basic model. The capability of the system for edge enhancement was first investigated by M. A. Vorontsov at US Army Research Lab (J. Opt. B Quant. Semi. Opt. 1, R1(1999)) . Fig.5 gives the simulation results. The image on the left is an infrared image input to the system, whereas the two on the right are the output. The latter are stationary state solutions of the system under different parameter conditions and show both edge enhancement and segmentation of different image parts.

Fig.5 Edge enhancement and segmentation. Image on the left is an infrared input image and the two in the middle and right are the output of the system.

In collaboration with QinetiQ Limited (UK), we have investigated this system for a potentially important military application. QinetiQ has been developing a real time correlation system for automatic target recognition and identification (ATRI) for the last 10 years. The correlator is similar to the classic VanderLugt correlator, but the input Fourier transform is performed electronically rather than optically. This novel "digital-plus-digital" architecture fully exploits the complementary benefits of optical and digital signal processors and results in a more compact and rugged structure than the VanderLugt correlator. The correlation is achieved by comparing the pre-installed templates with input images, so-called template matching. A correlation peak produced as a result of this process indicates the position of the target (or targets) in the image. The peak intensity shows the level of similarity between the target and the template. However, when the target is viewed against a cluttered background the correlation peak height is reduced significantly. In these situations, the correlation peak may "compete" with false peaks that may result from *non-important* objects present in the scene. The system will then be in danger of missing a positive identification or producing a large number of false identifications. In light of this an option is to minimise/remove the unwanted effect of the background and to enhance the features of interest in the images. For this purpose we have used our system as an image pre-processor for the correlator. Fig.6 shows a F16 aircraft and its edge enhanced image. The correlator shows an improved performance of target recognition when the edge enhancement image is used. We have further investigated images in more challenging environments with QinetiQ. Fig.7 shows a column of tanks in battle-field environment. The correlator is required to recognize their specific model in real time or quasi real time. However, on close inspection, these tanks have poorly defined edges. It seems to be a property of human visual system that we can see edges where in fact there are none (there is a smooth blend from the tanks to the background when one examines the pixels closely). We have performed a first test of the image using our system, images in the middle and on the right of Fig.7 are the output in different parameter conditions. A **g**eneral improvement of image contrast is observed. A test using these images is currently being undertaken at QinetiQ. The results from the test will be fed back for further system improvement.

Fig.6 Image edge enhancement . F16 aircraft (left) and its processed image (right)

Fig.7 edge enhancement operation. Original (left) and processed images (middle and right). Improvement of image contrast is observed.

PART TWO: Wavefront Sensing and Image Recovery

2.1 Introduction

The Zernike filter has over the last few years been investigated in a feedback loop for high-resolution wavefront sensing and control. Such adaptive systems were shown to be capable of compensating static phase distortion, with rapid convergence in a few iterations. In the meanwhile, nonlinear dynamical systems were proposed for real-time motion detection for its self-suppression of static background and enhancement of the contrast of moving objects. Here we study an adaptive Zernike dynamics feedback system by combining the capabilities of the Zernike wave front sensor with nonlinear dynamical systems for wave-front phasing. For an important application, we investigate such a system for phasing of a large telescope. Segmentation is considered as the most promising option for primary mirrors of more than 10m in diameter, but the segmentation of a primary mirror brings about specific problems associated with segment misalignment, such as piston, tip-tilt, etc. Phasing of these segmented surfaces therefore becomes a critical task for such a giant telescope. We show that our system can make use of a dynamical adaptation processing, which separate (static) misalignment of a segmented mirror from dynamical atmospheric turbulence.

2.2 System model

The Zernike filter was first proposed in 1955 for wavefront sensing by introducing a $\pi/2$ phase shift to the zero spatial frequency of an input light. The integration of the Zernike filter with an adaptive feedback system has led to new applications such as high-resolution wavefront compensation without the requirement of wavefront reconstruction. Recently, SLM has been used as a new means for realising the Zernike filter, which brings high resolution with flexibility, leading to different forms of Zernike filters. Among them is the differential Zernike filter, its output,

$$I_{diff}(r,t) = \frac{1}{2}[I_{diff}^{(+)}(r,t) - I_{diff}^{(-)}(r,t)]$$
$$= 2A_0(r)\,|\,\overline{A_0}(t)\,|\,\sin[u(r,t) + v(r,t) - \Delta], \tag{6}$$

of which has been shown to be proportional to the Stehl ratio gradient. The filter can be realised by using a controllable phase shift switching between $\pm\pi/2$, which offers a means for implementing direct-control adaptive optical systems by use of the gradient-flow optimisation paradigm.
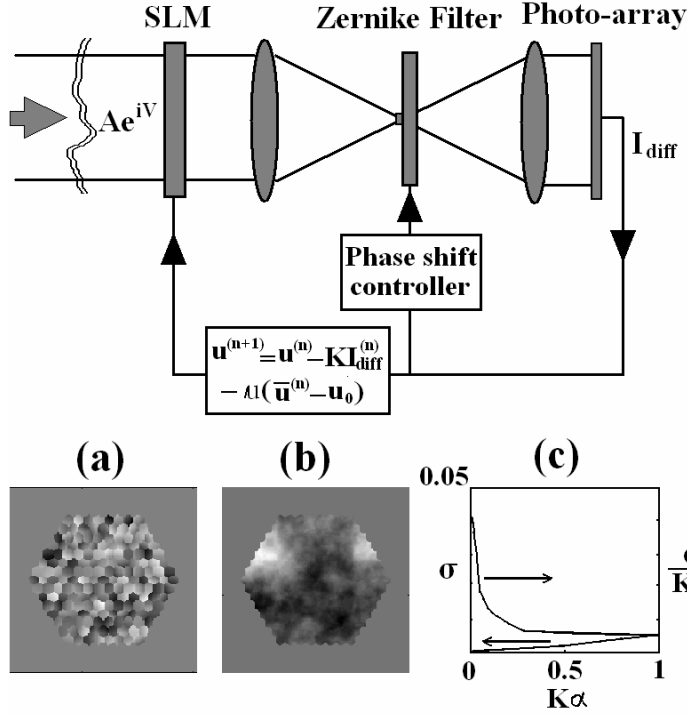
Fig. 8. Schematic of adaptive Zernike dynamical feedback system; the input phase v comprises error from misalignment mirror, v_m, and distortion from atmospheric turbulence, v_a; a snap shot of them are show in (a) and (b); (c) shows the relationship between $u_a^{(n)}$ and $K\alpha$; σ represents the standard deviation of $u_a^{(n)}$.

Fig. 8 shows the schematic of the adaptive Zernike dynamical feedback system, which comprises a phase spatial light modulator (SLM) as wavefront corrector and a differential Zernike filter as wavefront sensor, the two are coupled by a feedback loop. The system has previously been used for direct wave-front correction of a single image. In this study we will develop it for a different application for phasing of a static wave-front distortion in the presence of turbulence. Here the SLM introduces a phase modulation $u(r,t)$ to the distorted input wave $A_{in}(r,t) = A_0(r)\exp[iv(r,t)]$, where $v(r,t)$ is the phase distortion inside the telescope aperture, comprising both static misalignment of the segmented mirrors, $v_m(r)$, and time-dependent atmospheric turbulence, $v_a(r,t)$, i.e., $v(r,t) = v_m(r) + v_a(r,t)$. The corrected wave $A_{out}(r,t) = A_0(r)\exp\{i[u(r,t)+v(r,t)]\}$ is used as the input to the wavefront sensor. The output intensity $I_{diff}(r,t)$ from the sensor is then used to control the phase modulation $u(r,t)$ on the SLM. The system performance dynamics can be written in a continuously distributed model as,

$$\frac{\partial u(r,t)}{\partial t} = d\nabla^2 u(r,t) - KI_{diff}(r,t) - \mu[\overline{u}(t) - u_0] \tag{7}$$

where $\overline{u}(t) = S^{-1}\int u(r,t)d^2r$ is the phase averaged over the aperture area S; u_0 is a desirable value for $\overline{u}(t)$; d, K, and μ are coefficients. The discrete-time iteration equation,

$$u^{(n+1)}(r_{i,j}) = u^{(n)}(r_{i,j}) + d\nabla u^{(n)}(r_{i,j}) - KI_{diff}^{(n)}(r_{i,j}) - \mu[\overline{u}^{(n)} - u_0] \tag{8}$$

may be used to described Eq.7, where $n = 1,2,3,...$ is the iteration number.

2.3 Small signal analysis
The capability of Eq.8 for phasing of a segmented mirror in the presence of strong atmospheric turbulence lies

in its dynamical nature: compensation occurs only to signals whose dynamics is slower than that of the system. This can be understood by the following analysis in the weak signal limit. For simplicity we assume $d = 0$ and $\mu = 0$, for which Eq.8 becomes:

$$u^{(n+1)}(r) = u^{(n-1)}(r) - KI_{diff}^{(n-1)}(r) - KI_{diff}^{(n)}(r)$$

$$= u^{(n-2)}(r) - KI_{diff}^{(n-2)}(r) - KI_{diff}^{(n-1)}(r) - KI_{diff}^{(n)}(r) \tag{9}$$

$$= \cdots\cdots$$

$$= -K[I_{diff}^{(1)}(r) + I_{diff}^{(2)}(r) + \cdots + I_{diff}^{(n)}(r)].$$

Here $u^{(1)} = 0$ is assumed. In the weak signal limit, $\sin(v) \approx v$, so Eq.6 can be expressed as a linear sum of the contributions from the static and dynamical phase modulations

$$I_{diff}^{(n)}(r) \approx \alpha[u^{(n)}(r) + v^{(n)}(r)]$$

$$= \alpha[u_m^{(n)}(r) + v_m^{(n)}(r)] + \alpha[u_a^{(n)}(r) + v_a^{(n)}(r)], \tag{10}$$

where $u^{(n)}(r) = u_m^{(n)}(r) + u_a^{(n)}(r)$, $v^{(n)}(r) = v_m^{(n)}(r) + v_a^{(n)}(r)$, $\alpha = 2A_0 \mid \overline{A_0} \mid$ and Δ in Eq.6 is set to 0. Combining (9) and (10) leads to two equations that describes separately the feedback signals due to misalignment and atmospheric turbulence,

$$u_m^{(n+1)}(r) = [(1 - K\alpha)^n - 1]v_m(r) \tag{11}$$

$$u_a^{(n+1)}(r) = -K\alpha[(1 - K\alpha)^{n-1}v_a^{(1)} + (1 - K\alpha)^{n-2}v_a^{(2)}$$

$$+ \cdots + (1 - K\alpha)v_a^{(n-1)} + v_a^{(n)}]. \tag{12}$$

Eq.11 gives the known result in the absence of atmospheric turbulence; for $K\alpha < 1$, $u_m^{(n)}$ accumulates with the increase of the number of iteration and eventually converges to $-v_m$. However, $u_a^{(n)}$ behaves differently. When the interval between successive iterations is longer than the correlation time of atmospheric turbulence, $v_a^{(n)}$ is uncorrelated between different steps and $u_a^{(n)}$ does not accumulate in the way as $u_m^{(n)}$ does. In this case, the contribution to $u_a^{(n)}$ in Eq.(12) comes mainly from the last few terms in the polynomial, the number of terms that should be included depend on the values of $K\alpha(<1)$. We have calculated Eq.12 for different values of $K\alpha$ for sufficiently large n, in which $v_a^{(n)}$ is generated by the Kolmogorov model with the Fried parameter of 0.2m and varies randomly at every iteration. The normalised standard deviation of $u_a^{(n)}$, $\sigma^* = \sigma / \overline{\sigma_0}$, where $\overline{\sigma_0}$ is the standard deviation of the atmospheric distortion $v_a^{(n)}$ averaged over time, is shown to increases monotonically with the increase of $K\alpha$, as given in Fig.9(a). The total phase signal in the feedback loop is $u^{(n)} = -v_m + u_a^{(n)}$ for sufficiently large n. Therefore, $u_a^{(n)}$ can be regarded as the retrieved phase of the misaligned mirror on a noise background. If $K\alpha$ is chosen to be sufficiently small, the noise is also smaller compared with the retrieved signal. In a practical system, α is usually fixed and K can be varied as the electronic gain parameter. However, K also controls the convergent rate of the system, larger K results in faster convergence. So a balance between weak noise level and convergent rate should be considered in practical applications.
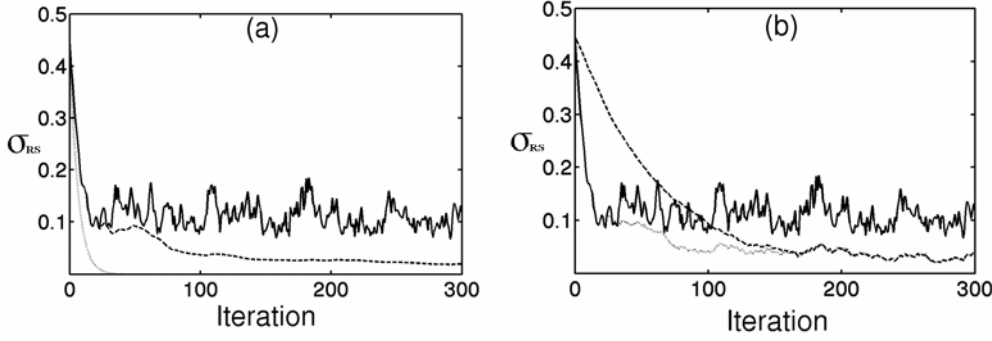
Fig.9 (a) The standard deviation (σ_{RS}) of the retrieved signal, $u^{(n)}$, against the actual misalignment, v_m, as a function of the iteration number; solid curve corresponds to $\pm 0.4\pi$ amplitude variation for both the misalignment, v_m, and atmospheric turbulence v_a; dash curve is the averaged σ_{RS} over many iterations; dotted curve corresponds to σ_{RS} in the absence of atmospheric turbulence. The feedback gain is set to be $K = 0.75$. (b) σ_{RS} for different feedback gains; $K = 0.75$ (solid), $K = 0.1$ (dash), and varying K (dot) : 0.75 for $n<20$ and 0.1 for $n>20$.

2.4 Numerical simulations

Now we study the performance of the system in the case of arbitrary input phase amplitude by directly iterating Eq.8. Our numerical findings support the above results under the weak signal approximation. Again, atmospheric turbulence is generated using the Kolmogorov model and varies randomly at every iteration. The wavefront tilt, which can be removed by other techniques, is neglected in our simulation. The mirror misalignment signal is computed using a 169-hexagon formation, each of which has a random piston and tip-tilt. A snap shot of the two signals is shown in Fig.8(b) and (c). Fig. 9 shows the simulation result for which a peak-to-valley amplitude of 0.8π is used for both $v_m(r,t)$ and $v_a(r,t)$. The difference between the retrieved and original phase is measured by the standard deviation, $\sigma_{RS} = \sqrt{\sum [(u+v_m)-(\overline{u}+\overline{v}_m)]^2}$. When the signal is perfectly recovered, $u = -v_m$. Here the term $(\overline{u}+\overline{v}_m)$ is used to compensate a trivial constant shift. As shown in Fig.9, $\sigma_{RS} < 0.01$ is achieved for ~ 20 iterations in the absence of atmospheric turbulence. When the turbulence is included, σ_{RS} fluctuates around $\sigma_{RS} = 0.1$, which shows a good recovery by compared with $\sigma = 0.45$ for the original signal, which corresponds to σ_{RS} at $n=0$. The presence of turbulence at this level does not appear to change the convergent rate of the system. To reduce the level of random fluctuation we can average $u^{(n)}$ over many iterations after the convergence has been achieved, i.e., $<u> = \frac{1}{n-m}\sum_{i=m}^{n} u^{(i)}$. We obtain $\sigma_{RS} = 0.03$ after $m=1000$. Fig.9 (b) shows the effects of feedback K on σ_{RS}. In general, with increase of K, the convergence rate increases, but so does the noise level caused by the atmospheric turbulence. To achieve fast convergence rate and high quality recovery at the same time, we can vary K during the iteration processing; an example is given in which it is reduced from $K=0.75$ to 0.1 after the convergence is achieved.
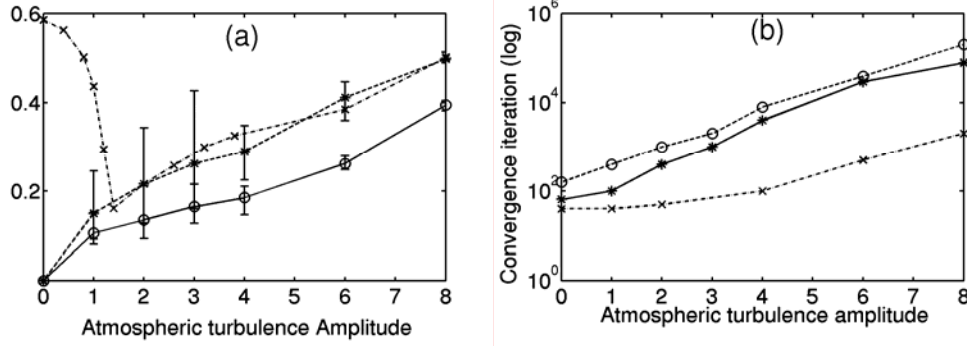
Fig.10 (a) standard deviation $<\sigma_{RS}'>$ versus different atmospheric turbulence amplitude (peak-to-valley), $K = 0.3$ (circle) and 0.75 (asterisk). (b) The number of iterations needed for convergence versus atmospheric turbulence amplitude for $K = 0.3$ (circle) and 0.75 (asterisk). The curves with cross corresponds to the results the Zernike filter with 5×5 pixel phase shift around the centre and for $K = 0.75$.

In a practical telescope system, atmospheric phase distortion increases with the diameter of the telescope aperture. For a segmented primary mirror with 8-10m diameter, the misalignment error is in the range of 4π peak-to-valley value whereas the atmospheric phase distortion is about 8π in the absence of tilt. We have examined the performance of the system for a fixed 4π phase misalignment, which corresponds to the standard deviation $\sigma = 2.24$, with varying atmospheric amplitudes from 0 to 8π. The results are evaluated by the standard deviation $\sigma_{RS}' = \sqrt{\sum[(u'+v_m) - (\overline{u'}+\overline{v}_m)]^2}$, where u' represents the phase image unwrapped from u. The phase wrap occurs because of the sine function in the Zernike filter. As σ_{RS}' fluctuates for each realisation, which is shown by the error bars in Fig.10(a), we average the results over 1000 iterations after the convergence of the system to obtain $<\sigma_{RS}'>$. Fig.10 (a) shows a monotonic increase of $<\sigma_{RS}'>$ with the atmospheric turbulence amplitudes for both feedback coefficients $K = 0.75$ and 0.3. Consistent with the weak signal analysis, we find that $<\sigma_{RS}'>$ is smaller for smaller values of K. As shown in this Fig.10(a), the standard deviation $<\sigma_{RS}'>$ is less than 20% of that of the misalignment for the atmospheric turbulence up to 8π, which indicates a good image recovery for the atmospheric turbulence amplitudes up to 2 times of that of the misalignment error. Fig.10(b) shows a monotonic increase of the numbers of iterations required for the system convergence with the atmospheric turbulence amplitudes. The increase is shown to be more dramatic when the atmospheric amplitude is greater than that of the misalignment error. Fig 10(b) also shows that a larger number of iteration is needed for larger feedback coefficient K, which also agrees with the weak signal analysis. Fig.11(a) is an example of a 4π misalignment phase error whereas Fig,11 (b) is the retrieved phase image in the presence of 8π atmospheric turbulence. A clear correspondence between the two images confirms the capability of the system.
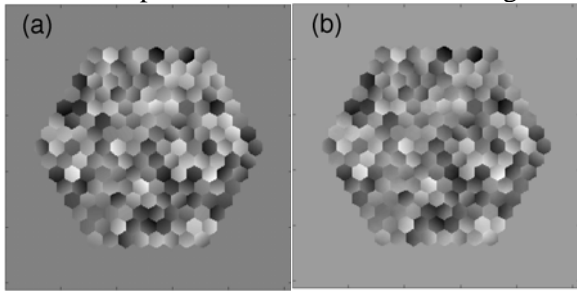

Fig. 11(a) The input phase distortion of a segmented mirror and (b) retrieved phase image. Here the peak-to-valley amplitude is 4π for the misalignment and 8π for atmospheric turbulence.

The slow convergence of the retrieved images in the case of large atmospheric turbulence amplitudes may cause problems for the application of our system to a large aperture telescope. When the atmospheric amplitude increases, the incoming images comprise more and more high spatial frequency components, which in turn reduces the probability of a bright speckle in the centre of the spectral plane. Consequently, the Zernike outputs for $\pm \pi/2$ phase shift, $I_d^{(+)}$ and $I_d^{(-)}$, become less different, which reduces the effect of the differential Zernike filter, leading to slower convergence. To overcome this problem, we have studied the system by enlarging the phase shift region in the spectral plane. Fig.10 gives the numerical results using the differential Zernike filter with phase shift of 5×5 pixels centred at the zero spectral component. As shown in Fig.10(b), the convergence rate is significantly increased, especially for larger atmospheric amplitudes where the increase is of two orders of magnitude. However, the standard deviation $<\sigma_{RS}'>$ using such a Zernike filter reveals a new feature, as shown in Fig.10(a). While $<\sigma_{RS}'>$ is similar to that obtained by the conventional Zernike filter for relatively large atmospheric amplitudes, it behaves very differently when the amplitudes are below the value of around π. This is because when the atmospheric amplitudes are low the incoming images comprise mainly the static misalignment. This leads to the build-up of a considerable amount of low spatial frequency components (slope effect) in the retrieved phase images by the Zernike filter with 5×5 pixels, which results in the increase of $<\sigma_{RS}'>$ in the small atmospheric amplitude region. When the images comprise a significant portion of dynamical component, the slope effect becomes less prominent and the results for the two cases with different pixel numbers are essentially the same. This study shows that we can choose Zernike filter with different pixels to achieve both good quality phase image recovery and fast convergence rate. The detailed analysis of this work will be presented in a separate report.

In conclusion, we have in part two studied an adaptive Zernike dynamical feedback system and shown by analysis and simulation that it provides an effective means to measure segment misalignment error in the presence of strong atmospheric turbulence. This system may be implemented in an optoelectronic device, which would provide a practical method for phasing of segmented mirror and other applications.

III. Future Work

This project has provided a solid base for the theory of SENDSs for nonlinear optical/optoelectronic image processing and has shown through analysis and modelling that SENDSs can be used for two key applications in both military and civil areas. Based on these results we are currently looking for further support from government agencies and industry from which lab demonstrations can be carried out.